ACS APPLIED MATERIALS & INTERFACES

www.acsami.org

Research Article

Why Hybrid Tin-Based Perovskites Simultaneously Improve the Structural Stability and Charge Carriers' Lifetime: Ab Initio Quantum Dynamics

Akang Li, Qi Liu, WeiBin Chu, WanZhen Liang,* and Oleg V. Prezhdo*

Cite This: *ACS Appl. Mater. Interfaces* 2021, 13, 16567−16575

Read Online

ACCESS | Metrics & More | Article Recommendations | Supporting Information

ABSTRACT: Much effort has been dedicated to boost the development of lead-free perovskite solar cells. However, their performance and stability are still much less competitive to the lead-bearing counterparts. By exploiting a mixed Sn−Ge cation strategy for the development of lead-free perovskites, we perform ab initio electronic structure calculations and quantum dynamics simulations on $MASn_{0.5}Ge_{0.5}I_3$ and compare them to $MASnI_3$. The calculations demonstrate that the hybrid cation strategy can improve simultaneously the perovskite stability and the lifetime of charge carriers. The stability increases due to a larger space of possible structures within the favorable range of the structural parameters, such as the Goldschmidt tolerance and octahedron factors. By exploring the larger structure space, mixed perovskites find stable configurations with lower free energies and better fitting components that exhibit reduced fluctuations around the equilibrium geometries. Charge carriers live longer in mixed perovskites because cation mixing results in an additional and moderate disorder that separates electrons and holes, reducing their interactions while still maintaining efficient band-like charge transport. These general and fundamental principles established by the analysis of the simulation results are useful for the design of advanced materials for solar energy and construction of optoelectronic devices.

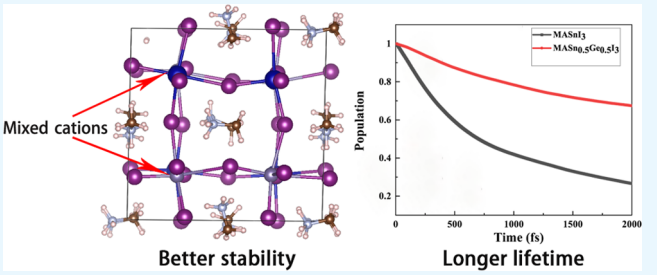

KEYWORDS: *double metal halide perovskites, solar cells, geometric and electronic structure, nonadiabatic molecular dynamics, time-dependent density functional theory*

1. INTRODUCTION

Perovskite solar cells (PSCs) have long been one of the most popular photovoltaic research hotspots in the past decade due to their excellent performance, easy synthesis, and low cost.[1−17] Their certified power conversion efficiency (PCE) increased rapidly to over 24%;[18−21] while lead-based PSCs are highly efficient, the toxicity of lead (Pb) and their poor long-term device stability hinder their large-scale commercialization. Furthermore, Pb halide perovskites exhibit band gaps that are typically not within the optimal range for single-junction solar cells (SJSCs) according to Shockley−Queisser's theory. Thus, it is an urgent need to find alternatives.

Partial or complete lead replacement with other metal atoms is gaining increasing interest, due to the requirements of narrowing the band gaps further and reducing PSCs' impact on the environment. In the fields of developing lead-free perovskites,[6,17,22−24] the earliest strategy was to replace Pb with group 14 elements, such as Sn and Ge.[18,25,26] Tin-bearing halide perovskites enable the fabrication of lead-free PSCs, ideal utilization of solar spectrum in single-junction cells, and construction of tandem all-perovskite solar cells. However, tin-bearing halide perovskites suffer from easy oxidation of Sn^{2+} to Sn^{4+} by oxygen once exposed to air, leaving oxidized vacancy defects. Such a characteristic makes the stability and performance of tin-based PSCs much less competitive to the lead-based PSCs.[27,28] $MAGeI_3$ (MA = CH_3NH_3) owns a wide band gap at about 2.0 eV and is difficult to synthesize, and PSCs based on $MAGeI_3$ show quite low PCE (often less than 0.6%).[29−31] Cation transmutation provides another strategy to design Pb-free and stable halide perovskites for solar energy applications. For the heterovalent substitution, two divalent Pb^{2+} ions are converted into monovalent M^+ and trivalent M^{3+} ions. The strategy produces a rich class of double perovskite structures of quaternary halides. Pb-free all-inorganic double perovskites have been synthesized successfully by heterovalent substitution with monovalent Au, Ag, Cu, alkalies, trivalent Bi, Sb, In, and rare-earth ions.[32−46] The optoelectronic properties of these double perovskites can be widely tuned. At the same time, double perovskites, such as those based on Ag−Bi and

Received: February 17, 2021
Accepted: March 23, 2021
Published: April 1, 2021

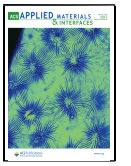

Ag−Sb cores, exhibit indirect band gaps and tend to dissipate light energy into heat in solar energy applications.[37−39,47−49]

On account of the significant shortcomings of the heterovalent double perovskites, the scientists turned to improve tin-based PSCs by adopting the B-site coalloying strategy, such as the creation of the mixed Sn−Ge or Sn−Pb metal core.[50−60] Pb-free mixed Sn−Ge perovskites have bright prospects for not only efficient and stable SJSCs but also efficient all-perovskite monolithic tandem solar cells. Several works have been devoted to develop these kinds of Pb-free materials. For example, Ju et al. suggested several mixed halide perovskites using Sn and Ge with suitable direct band gaps for light absorbers in solar cells from the first-principles calculations.[61] Ma et al. performed an exhaustive research on the mixed vacancy inorganic double perovskite $Cs_2Sn_{(1-x)}Ge_xI_6$, suggesting that the concentration of the Ge dopant will significantly affect the electronic, mechanical, and thermodynamic properties.[52] Ito et al. reported that PCE of $FA_{0.75}MA_{0.25}Sn_{(1-x)}Ge_xI_3$-based solar cells when the content of Ge x = 0.05 has reached 4.48%.[62] Liu et al. showed the first synthesis of $CsSn_{0.6}Ge_{0.4}I_3$ perovskite nanocrystals with a fine size distribution and found that the photophysical properties of $CsSn_{0.6}Ge_{0.4}I_3$ were enhanced considerably compared to those of Sn-based nanocrystals, which was attributed to prolonged charge carrier lifetimes.[51]

Although these theoretical and experimental works demonstrated that Ge doping in Sn-based PSCs in a small concentration can remarkably improve the PCE, the microscopic understanding of the static and dynamics characteristics of the materials is lacking. Here, we perform a first-principles density functional theory (DFT) combined with nonadiabatic molecular dynamics (NAMD) investigation on the mixed cation Sn−Ge perovskite material $MASn_{0.5}Ge_{0.5}I_3$ and obtain detailed insights guiding the construction of high-performance PSCs.

2. COMPUTATIONAL DETAILS

The calculations are carried out with Vienna Ab Initio Simulation Package (VASP 5.4),[63−65] using the projector augmented wave method with an energy cutoff of 550 eV. Unless otherwise specified, the generalized gradient approximation exchange-correlation functional Perdew−Burke−Ernzerhof (PBE)[65] is adopted in the calculations. Since PBE tends to underestimate band gaps, we employed the HSE06 functional[66] for benchmark calculations. HSE06 includes a fraction of screened HF exchange, α = 0.2, improving the discontinuity in the Kohn−Sham potential derivative for integer numbers of electrons. A 2 × 2 × 2 Γ-centered k-point grid is used for the structure optimization and a 4 × 4 × 4 k-point mesh is used for electronic structure calculations. Since the structures have direct band gaps located at the Γ-point, the NA couplings (NAC) are computed for the Γ-point only.

Once the geometry optimization is finished, the repeated velocity rescaling increases the temperature to 300 K and equilibrates the structures for 5 ps. Then, 10 ps adiabatic MD trajectories are obtained within the microcanonical ensemble with the MD time step set to 1 fs. Before the NAMD simulations, we need to compute the strength of NA couplings d_{ij} using the time-domain numerical method, and the overlap between two orbitals i and j in the time step order can be expressed as[67]

$$d_{ij} = -i\hbar\langle\phi_i|\nabla_{\mathbf{R}}|\phi_j\rangle\cdot\dot{\mathbf{R}} = -i\hbar\left\langle\phi_i\left|\frac{\partial}{\partial t}\right|\phi_j\right\rangle = -i\hbar\frac{\langle\phi_i(t)|\phi_j(t+\Delta t)\rangle - \langle\phi_i(t+\Delta t)|\phi_j(t)\rangle}{2\Delta t} \quad (1)$$

It is known that the strength of NA coupling has a directly proportional relationship with the overlap of the initial state i and the final state j, $-i\hbar\langle\phi_i|\nabla_R|\phi_j\rangle$, and the nuclei velocity, dR/dt. At last, the final 7000 configurations of the MD trajectories are selected as initial geometries for the following NAMD simulation including the electron−hole nonradiative recombination and relaxation dynamics in the conduction bands of the structures with Python Extension for Ab Initio Dynamics (PYXAID) code.[68,69]

3. RESULTS AND DISCUSSION

3.1. Electronic and Geometric Structures of $MASnI_3$ and $MASn_{0.5}Ge_{0.5}I_3$. First of all, to determine which kind of arrangement of Sn and Ge in formula $MASn_{0.5}Ge_{0.5}I_3$ is most stable, we construct a series of Sn−Ge mixed perovskite structures, as shown in Figure S1. We optimize their geometries and calculate their energies (Table S1). We find that configuration b in Figure S1, which is the same as the structure in Figure 1, possesses the lowest energy. The

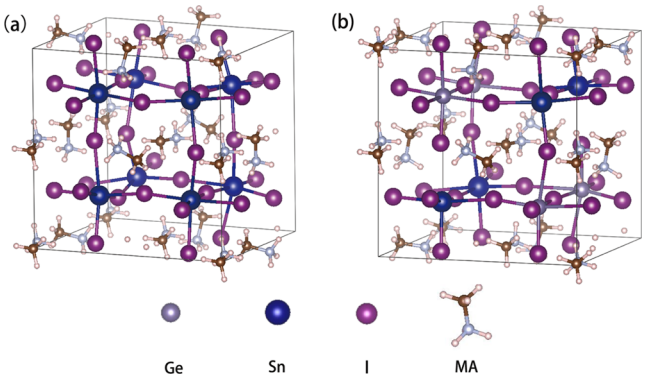

Figure 1. Optimized geometries of $MASnI_3$ (a) and $MASn_{0.5}Ge_{0.5}I_3$ (b).

computed free energies for $MASn_{0.5}Ge_{0.5}I_3$, $MASnI_3$, and $MAGeI_3$ are −406.6764, −406.3726, and −406.9190 eV, respectively. The formation energy of $MASn_{0.5}Ge_{0.5}I_3$ can thus be determined as −0.0306 eV according to $E_{form} = E_{MASn_{0.5}Ge_{0.5}I_3} - 0.5E_{MASnI_3} - 0.5E_{MAGeI_3}$, suggesting that the hybrid $MASn_{0.5}Ge_{0.5}I_3$ has better stability than pristine $MASnI_3$. We thus choose this configuration for the subsequent calculations.

Generally, the octahedral factor (μ) and the Goldschmidt tolerance factor (t) and are usually used as empirical indicators to assess the stability of the considered hybrid perovskites if they have the formula ABX_3.[70−72] The calculated tolerance factors for both $MASnI_3$ and $MASn_{0.5}Ge_{0.5}I_3$ indicate that they form cubic structures. The octahedral factor of $MASn_{0.5}Ge_{0.5}I_3$ deviates a bit from the favorable value, indicating that the $[GeI_6]^{4-}$ octahedra are tilted, and the perovskite tends to form a trigonal structure from the tetragonal one. The octahedral and Goldschmidt tolerance factors for pristine $MAGeI_3$ are also included for comparison. Hybrid $MASn_{0.5}Ge_{0.5}I_3$ can form a stable cubic structure similar to $MASnI_3$. However, if the content of Ge continues to increase, the structure of the hybrid

https://doi.org/10.1021/acsami.1c03145
ACS Appl. Mater. Interfaces 2021, 13, 16567−16575

perovskite will become more similar to $MAGeI_3$, which exhibits the less stable trigonal perovskite structure, indicating that the content of Ge in the hybrid perovskite should be kept under 0.5 to ensure better structural stability.

Considering that the temperature in our MD and NAMD simulations is set to 300 K, at which $MASnI_3$ would exhibit the tetragonal perovskite structure, we adopt a 96 atoms 2 × 2 × 2 cubic supercell with tetragonal perovskite structures in the calculations. The calculated main geometric parameters are shown in Table 1. The calculated bond length average value of

Table 1. Main Geometric Parameters of $MASnI_3$, $MASn_{0.5}Ge_{0.5}I_3$, and $MAGeI_3$[a]

structure	$MASnI_3$	$MASn_{0.5}Ge_{0.5}I_3$	$MAGeI_3$
a (Å)	12.74	12.78	12.74
b (Å)	12.63	12.52	12.36
c (Å)	12.67	12.57	12.49
α	90.82	89.44	90.36
β	89.67	88.39	87.00
γ	89.22	89.18	89.41
$\overline{R}_{Sn-I}$ (Å)	3.21	3.22	
$\overline{R}_{Ge-I}$ (Å)		3.16	3.17
∠I−Sn−I (deg)	163.84−177.98	166.37−179.12	
∠I−Ge−I (deg)		159.27−172.11	161.75−172.16
band gap (PBE)	1.15	1.28	
band gap (HSE06 + SOC)	1.37	1.68	

[a]Band gaps (in eV) are calculated by DFT with PBE and HSE06 + SOC.

Sn−I is 3.21 Å in the $MASnI_3$ system, exhibiting good consistency with the earlier DFT calculated values, ranging from 3.07 to 3.31 Å.[73] We find that the decrease of the M−I (M is Sn or Ge) bond length and the smaller M−I bond distortion compared to those in pristine $MASnI_3$ result in $MASn_{0.5}Ge_{0.5}I_3$ having a smaller volume, and thus better stability, which can be further confirmed from the MD simulations.

Figure 2 shows the computed density of states (DOS) and projected DOS (pDOS) (top panel) and charge densities of the pivotal states involved in the process of electron−hole recombination of $MASnI_3$ and $MASn_{0.5}Ge_{0.5}I_3$. The DOS contributions for $MASnI_3$ are divided into MA(C, H, N), Sn, and I components (Figure 2b). As for $MASn_{0.5}Ge_{0.5}I_3$, the contribution of the Ge component to pDOS is included, together with the components in $MASnI_3$ (in Figure 2a). Figure 2a shows that the valence band maximum (VBM) of $MASnI_3$ comprises I 5p as well as Sn 5s5p electrons, but its conduction band minimum (CBM) is attributed to Sn 5p and I 5p electrons (also see Figure S2a). Figure 2b demonstrates the pDOS of $MASn_{0.5}Ge_{0.5}I_3$. The valence band close to the gap is formed mainly by I 5p electrons, with a minor contribution of Sn-5s and Ge-4s electrons. Meanwhile, the conduction band involves Sn 5p and Ge 4p contributions, with negligible I 5p contribution. Figure 2c,d shows the charge densities of the VBMs and CBMs. It is notable that the charge densities of $MASn_{0.5}Ge_{0.5}I_3$ in the VBM and the CBM are more localized compared to those of $MASnI_3$, indicating better-separated electrons and holes, which should suppress the charge recombination and improve the carriers' lifetimes.

The band gap has a great influence on the process of electron−hole recombination since the NA coupling is inversely proportional to the band gap, and the recombination rate is proportional to the square of the coupling, in the light of Fermi's golden rule. We thus calculated the band gaps by the more advanced HSE06 functional including the spin−orbital coupling (SOC) effect. The band gaps of $MASnI_3$ calculated by PBE and HSE06 + SOC are 1.15 and 1.37 eV, which are in good consistency with the earlier reported value of 1.30 eV.[74] The band gaps of $MASn_{0.5}Ge_{0.5}I_3$ are 1.28 eV according to PBE and 1.68 eV according to HSE06 + SOC. Although the PBE functional typically underestimates the band gaps of the two materials, it maintains the trend of the band gap difference between $MASnI_3$ and $MASn_{0.5}Ge_{0.5}I_3$.

The band structures computed in this study are shown in Figure S5 in the Supporting Information (SI). We observe that in $MASn_{0.5}Ge_{0.5}I_3$, the valence band states near the band edge

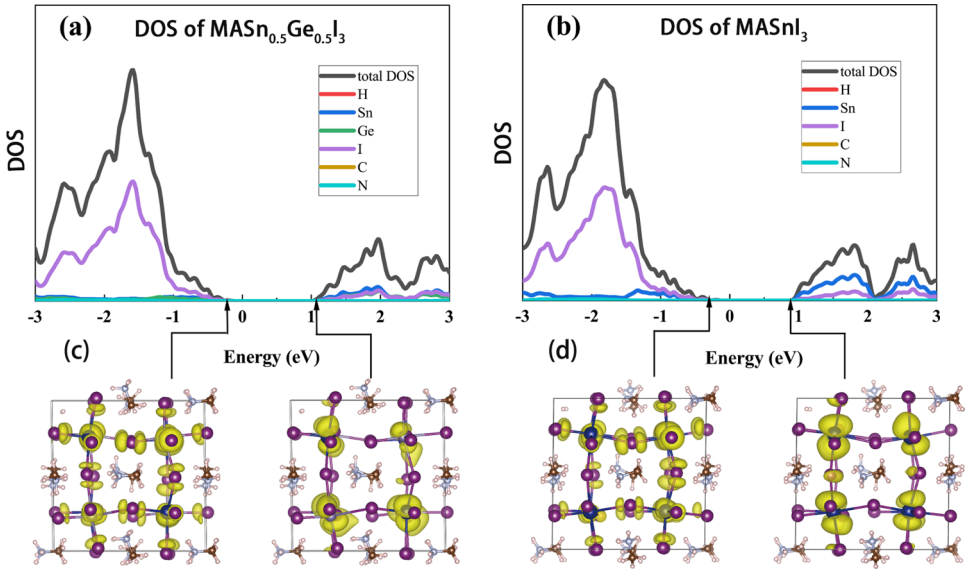

Figure 2. DOS and pDOS of (a) $MASn_{0.5}Ge_{0.5}I_3$ and (b) $MASnI_3$. The charge density distribution of the VBM and the CBM for (c) $MASn_{0.5}Ge_{0.5}I_3$ and (d) $MASnI_3$.

https://doi.org/10.1021/acsami.1c03145
ACS Appl. Mater. Interfaces 2021, 13, 16567−16575

Table 2. Standard Deviations (Å) of Atomic Positions and Sn−I and Ge−I Bond Lengths in $MASnI_3$ and $MASn_{0.5}Ge_{0.5}I_3$ at 300 K

	total[a]	MA[b]	I	Sn	Ge	Sn−I	Ge−I
$MASnI_3$	1.5685	1.8484	0.6817	0.3948		0.6314	
$MASn_{0.5}Ge_{0.5}I_3$	1.4551	1.7097	0.6601	0.3606	0.3186	0.6391	0.6389

[a]Averaged over all atoms of the systems. [b]Averaged over atoms in MA.

become relatively closer to the VBM, especially for VBM-1 and VBM-2, while the conduction band states move farther away from the CBM.

3.2. Thermal Structure Fluctuation and Carrier Lifetimes of $MASnI_3$ and $MASn_{0.5}Ge_{0.5}I_3$. To characterize the thermal influence on the stability of $MASnI_3$ and $MASn_{0.5}Ge_{0.5}I_3$, we compute each type of atoms' standard position deviation and average them canonically in line with the formula $\sigma_i = \sqrt{\langle(\vec{r}_i - \langle\vec{r}_i\rangle)^2\rangle}$, where $\vec{r}_i$ stands for the position of the ith atom on the generated MD trajectories and the angular brackets represent averaging canonically. The data are separated into the MA, I, Sn, or Ge components in both studied systems, helping to characterize their stability and demonstrate the cause of the differences. The calculated results are shown in Table 2. The standard deviations of I, MA, and Sn atoms in $MASn_{0.5}Ge_{0.5}I_3$ are smaller than those in $MASnI_3$, while the fluctuation of the Sn−I bond length in $MASnI_3$ is smaller than that in $MASn_{0.5}Ge_{0.5}I_3$, in which I atoms residing between Sn and Ge are biased toward Ge. In spite of a slight increase in the Sn−I bond length in $MASn_{0.5}Ge_{0.5}I_3$, the standard deviations for overall atomic positions in the mixed Sn−Ge perovskite are lower than those in $MASnI_3$, indicating that Ge-bearing $MASn_{0.5}Ge_{0.5}I_3$ has a more robust structure and should exhibit better thermal stability.

The spectral density characterizes the magnitude of the electron−phonon couplings and identifies the frequencies of the phonon modes, which directly couple to the charge carriers. Figure 3 shows the spectral densities for the electron−hole recombination process, calculated by performing Fourier transforms of the band gap fluctuations, $C_{ij}(t) = \langle\delta E_{ij}(t')\delta E_{ij}(t - t')\rangle_{t'}$, where the angular brackets represent an equilibrium ensemble average over the MD trajectories, and $\delta E_{ij}(t)$ denotes the fluctuation of the energy gap between states i and j. As shown in Figure 3, the low-frequency vibrations within the 20−500 cm^{-1} range are present in the spectral densities. The magnitude of the signal decreases with the increasing frequency. The dominant peak in $MASnI_3$ can be assigned to the octahedral twist motion at 40.33 cm^{-1}, and the minor peak just near the major mode can be ascribed to the Sn−I bending motion at 80.66 cm^{-1}.[75] The second peak located at 120.98 cm^{-1} can be assigned to the Sn−I stretching mode.[75] The peak close to 200 cm^{-1} is usually considered as the libration mode of organic cations according to the previous calculations.[76] Librations of the organic cations have an indirect impact on the NA coupling between the VBM and the CBM since the cations do not contribute to the DOS near the band gap. Compared with pristine $MASnI_3$, the dominant peaks arising from $[SnI_6]^{4-}$ and $[GeI_6]^{4-}$ vibrations in $MASn_{0.5}Ge_{0.5}I_3$ are reduced. The result is consistent with the values of standard deviations reported in Table 1.

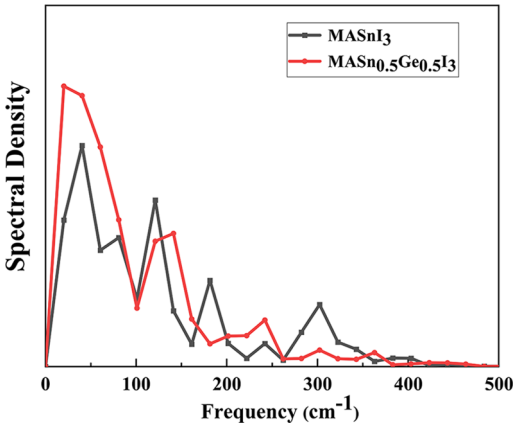

Figure 3. Spectral densities determined as Fourier transforms of autocorrelation functions of the band gap fluctuations.

Charge distributions of the key electronic states provide insights into the strength of the electron−hole interaction. Since the charge distributions obtained for the optimized geometries (Figure 2) do not always represent the properties of the system at ambient conditions, we characterized localization of the electronic states along the MD trajectories at 300 K. In particular, we evaluated the inverse participation ratio (IPR) for both the VBM and the CBM along the MD trajectories. The IRP[77,78] is calculated as $\mathrm{IPR} = N\frac{\sum k_i^4}{(\sum k_i^2)^2}$ IPR ∈ (0, 1), where N denotes the sum of total grid points, while k_i stands for the charge density in the volume of the ith unit grid. If the IPR value is larger, the charge distribution will be more localized. IPR = 1 means a completely localized state. Figure 4 shows that Ge doping in $MA(SnGe)_{0.5}I_3$ increases the CBM's IPR values compared to $MASnI_3$ by a notable degree, while the difference in the VBM

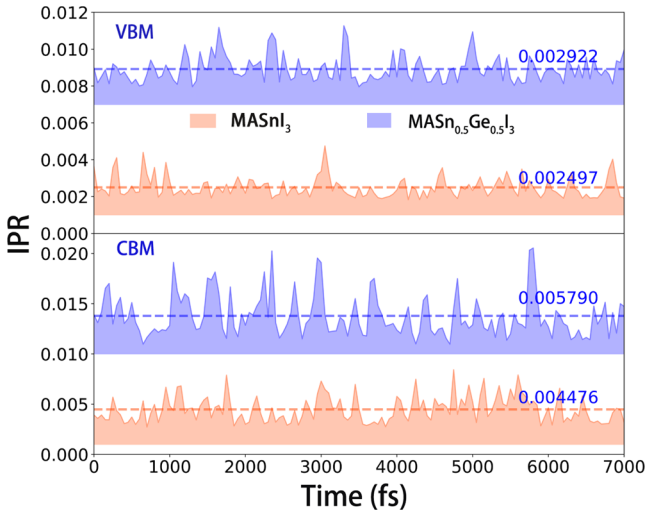

Figure 4. Inverse participation ratio for the VBM and CBM charge densities along the MD trajectories for $MASnI_3$ and $MASn_{0.5}Ge_{0.5}I_3$. The average values are shown by the dashed lines.

https://doi.org/10.1021/acsami.1c03145
ACS Appl. Mater. Interfaces 2021, 13, 16567−16575

is smaller. This is because the CBM is supported by Sn and Ge atoms, and their mixing created additional disorder and localization. The VBM is supported by I atoms, and therefore, it is not much influenced by the Sn−Ge mixing. The higher localization of the electronic states corresponds to a higher degree of separation of electrons and holes and weaker NA coupling (see Table 3).

Table 3. Pure-Dephasing Time (T_{pd}), Averaged Absolute Value of NA Coupling (NAC), and Nonradiative Charge Recombination Time (T_{rec}) of $MASnI_3$ and $MASn_{0.5}Ge_{0.5}I_3$

system	NAC (meV)	T_{pd} (fs)	T_{rec} (ns)
$MASnI_3$	0.69	8.17	8.67
$MASn_{0.5}Ge_{0.5}I_3$	0.60	6.63	22.71

Figure 5 visualizes the NA couplings between ten orbitals around the band edges. The NA coupling magnitudes increase from blue to red. These matrix heat maps indicate that the largest NA coupling arises directly between states that are close to each other. The NA coupling between the VBM and the CBM is smaller than the coupling between neighboring orbitals inside the valence and conduction bands. The large intraband couplings favor a rapid relaxation process of the charge carriers to the band edges, where they live for a long time prior to the nonradiative recombination. Carriers deeper inside bands, so-called hot carriers, typically exhibit larger diffusion lengths. The data of Figure 5 indicate that the intraband couplings are smaller in the valence band than those in the conduction band, suggesting that holes can remain hot for a longer time than electrons.

Next, we calculate the pure-dephasing times for the important process of the CBM−VBM transition. The pure-dephasing times characterize the duration of coherence formed between the states during the nonradiative transition. Figure 6a shows the definition of the pure-dephasing functions, $D_{ij}(t) = \exp\left(-\frac{1}{\hbar^2}\int_0^t dt' \int_0^{t''} dt'' C_{ij}(t'')\right)$, calculated through the double integration of the unnormalized autocorrelation functions (un-ACF) in line with the phonon-induced fluctuation of the VBM−CBM band gap, $C_{ij}(t) = \langle \delta E_{ij}(t')\delta E_{ij}(t - t')\rangle_{t'}$, according to the second-order cumulant approximation of the optical response theory.[79] The pure-dephasing times shown in Table 2 can be computed through fitting in the Gaussian function, $\exp[-0.5(t/\tau)^2]$. In general, a larger initial value of the system's un-ACF gives faster pure dephasing. The un-ACF initial value with the formula $C_{ij}(0) = \delta E_{ij}^2(0)$ gives the square of the band gap fluctuation. The value enters the pure-dephasing functions in front of the double integral. Comparing the data in Tables 2 and 3, we find that the initial values of un-ACF are consistent with atomic fluctuations.

The mixed Sn−Ge perovskite $MASn_{0.5}Ge_{0.5}I_3$ exhibits a smaller pure-dephasing time, corresponding to a longer carrier lifetime. Generally, shorter pure-dephasing times lead to correspondingly slower dynamics as exemplified by the quantum Zeno effect.[80] The pure-dephasing time of the mixed perovskite is shorter because its states are more disordered and localized and therefore are less correlated. Thus, a moderate amount of disorder is favorable for longer carrier lifetimes. While the significant disorder can extend carrier lifetimes even more, it can have a negative impact on carrier diffusion.

Figure 6b displays the evolution of the excited state population in $MASnI_3$ and $MASn_{0.5}Ge_{0.5}I_3$. To determine the timescale of the electron−hole recombination, τ, we fit the 2000 fs data from NAMD to the exponential decay according to the short-time approximation, i.e., $P(t) = \exp(-t/\tau) \approx 1 - t/\tau$. The recombination time scales are presented in Table 2. The charge carrier lifetime is nearly 3 times longer in the mixed cation Sn−Ge perovskite, compared to its counterpart with a single metal cation. This is because the charge carriers are more localized in the mixed perovskite and overlap and interact less. The larger localization leads to the faster pure dephasing and thus smaller NA coupling for the process of the CBM−VBM transition in $MASn_{0.5}$ $Ge_{0.5}I_3$. The NA coupling together with the pure-dephasing time is the main characteristic that governs the transition time in the NAMD calculation. To compare the lifetimes of hot electrons in the pure and mixed perovskites, we studied the relaxation of the electron from CBM + 1 to the CBM (Figure 6c). The data show that the hot electron relaxation is slower in $MASn_{0.5}Ge_{0.5}I_3$ than that in $MASnI_3$, also because of the smaller NA coupling, originating from the more significant localization of the electron in the mixed perovskite.

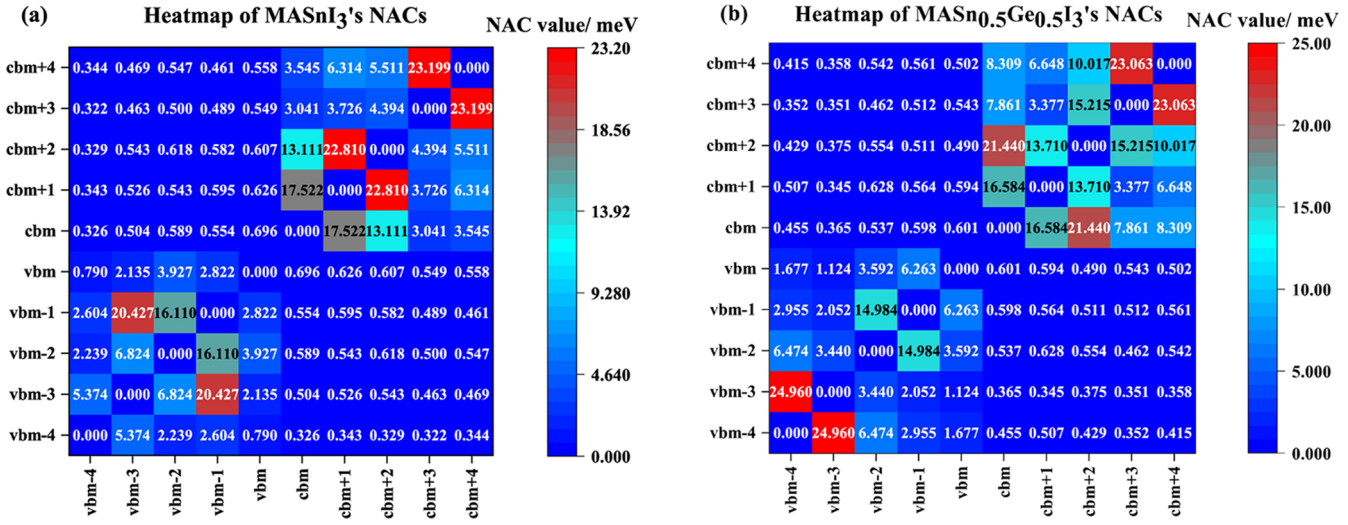

Figure 5. Heat maps of the NA coupling matrix for (a) $MASnI_3$ and (b) $MASn_{0.5}Ge_{0.5}I_3$.

https://doi.org/10.1021/acsami.1c03145
ACS Appl. Mater. Interfaces 2021, 13, 16567−16575

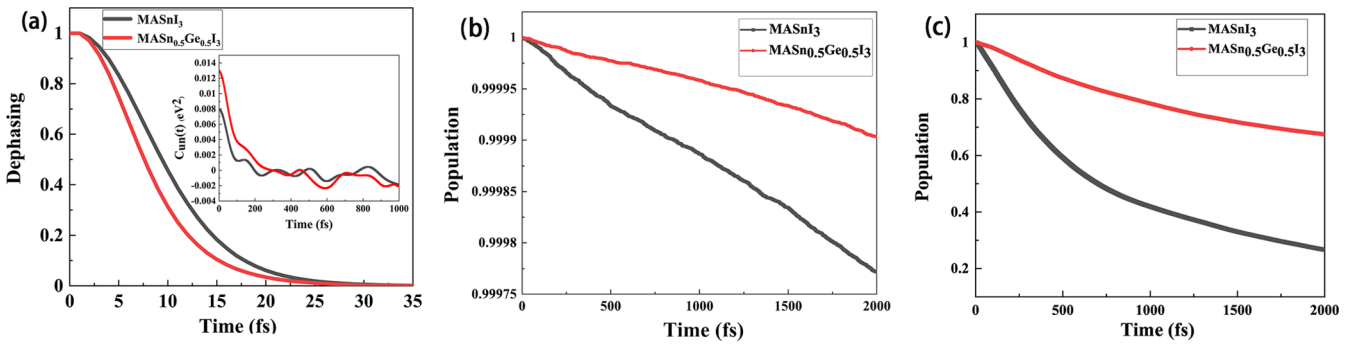

Figure 6. (a) Computed pure-dephasing functions and corresponding un-ACF (inset). (b) Electron−hole nonadiabatic recombination dynamics in $MASnI_3$ and $MASn_{0.5}Ge_{0.5}I_3$. (c) Relaxation dynamics from CBM + 1 to CBM in $MASnI_3$ and $MASn_{0.5}Ge_{0.5}I_3$.

4. CONCLUSIONS

We have performed a first-principles DFT study combined with the NAMD simulations on the static and dynamic characteristics of the mixed Sn−Ge perovskite $MASn_{0.5}Ge_{0.5}I_3$ and compared the mixed perovskite with its pristine counterpart $MASnI_3$. The study reveals how the Ge dopant influences the electronic and geometric properties of the perovskite at 0 K and ambient temperature, including the bond lengths, atomic fluctuations, Goldschmidt tolerance and octahedron factors, band gaps, electronic−vibrational coupling, elastic electron−phonon scattering time, hot carrier relaxation times, and times of the nonradiative electron−hole recombination process. The results demonstrate that even with a large proportion of the Ge content, the mixed Sn−Ge perovskite exhibits better stability in the desired structural form and longer-lived charge carriers. The analysis of the simulation data establishes the microscopic mechanism of the prolonged carriers' lifetime of $MASn_{0.5}Ge_{0.5}I_3$. The following conclusions can be drawn according to this study: (1) $MASn_{0.5}Ge_{0.5}I_3$ is more structurally stable than $MASnI_3$, as evidenced by the lower free energy, smaller atomic fluctuations, and decreased Sn(Ge)−I bond lengths. (2) The intraband relaxation of hot charge carriers occurs on a picosecond timescale, with hot electrons having longer lifetimes in $MASn_{0.5}Ge_{0.5}I_3$ than $MASnI_3$. Hot charge carriers exhibit faster diffusion that is favorable for solar cell applications. (3) $MASn_{0.5}Ge_{0.5}I_3$ shows a notable reduction of the NA coupling among the band edge states and a decrease in the corresponding pure-dephasing time. Consequently, the nonradiative recombination of charge carriers across the band gap is slowed down by a factor of 2.6. The improved properties of the mixed perovskite, compared to its pristine counterpart, arise from the additional and modest disorder induced by the cation mixing. A modest degree of disorder reduces the overlap of electrons and holes and decreases their interaction, without undermining long-range charge diffusion, which can drop significantly if the disorder is large. The work demonstrates that even for the large proportion of cation mixing, the hybrid perovskite still has good stability and longer carriers' lifetime due to the suppressed fluctuations of atoms, and the reduced NA couplings between the CBM and the VBM. Our study has provided an atomistic perspective to the relationship between the structure and electronic properties, especially the charge dynamics in mixed perovskites and has generated valuable insights that can be used to design lead-free perovskites for optoelectronic and solar energy devices.

ASSOCIATED CONTENT

Supporting Information

The Supporting Information is available free of charge at https://pubs.acs.org/doi/10.1021/acsami.1c03145.

Geometric structures of different configurations; their free energies; Goldschmidt tolerance and octahedron factors; and projected densities of states and band structures of $MASn_{0.5}Ge_{0.5}I_3$ (PDF)

AUTHOR INFORMATION

Corresponding Authors

WanZhen Liang − *State Key Laboratory of Physical Chemistry of Solid Surfaces, Collaborative Innovation Center of Chemistry for Energy Materials, Fujian Provincial Key Laboratory of Theoretical and Computational Chemistry, and Department of Chemistry, College of Chemistry and Chemical Engineering, Xiamen University, Xiamen, Fujian 361005, People's Republic of China;* orcid.org/0000-0002-5931-2901; Email: liangwz@xmu.edu.cn

Oleg V. Prezhdo − *Department of Physics and Astronomy, University of Southern California, Los Angeles, California 90089, United States; Department of Chemistry, University of Southern California, Los Angeles, California 90089, United States;* orcid.org/0000-0002-5140-7500; Email: prezhdo@usc.edu

Authors

Akang Li − *State Key Laboratory of Physical Chemistry of Solid Surfaces, Collaborative Innovation Center of Chemistry for Energy Materials, Fujian Provincial Key Laboratory of Theoretical and Computational Chemistry, and Department of Chemistry, College of Chemistry and Chemical Engineering, Xiamen University, Xiamen, Fujian 361005, People's Republic of China*

Qi Liu − *State Key Laboratory of Physical Chemistry of Solid Surfaces, Collaborative Innovation Center of Chemistry for Energy Materials, Fujian Provincial Key Laboratory of Theoretical and Computational Chemistry, and Department of Chemistry, College of Chemistry and Chemical Engineering, Xiamen University, Xiamen, Fujian 361005, People's Republic of China*

WeiBin Chu − *Department of Physics and Astronomy, University of Southern California, Los Angeles, California 90089, United States; Department of Chemistry, University of Southern California, Los Angeles, California 90089, United States;* orcid.org/0000-0001-5951-0337

Complete contact information is available at:

https://pubs.acs.org/10.1021/acsami.1c03145

Notes

The authors declare no competing financial interest.

■ ACKNOWLEDGMENTS

Financial support from the National Science Foundation of China (Grant No. 21833006) and the USA National Science Foundation (Grant No. CHE-1900510) is acknowledged.

■ REFERENCES

(1) Cho, C.; Palatnik, A.; Sudzius, M.; Grodofzig, R.; Nehm, F.; Leo, K. Controlling and Optimizing Amplified Spontaneous Emission in Perovskites. *ACS Appl. Mater. Interfaces* **2020**, *12*, 35242−35249.
(2) Zibouche, N.; Islam, M. S. Structure-Electronic Property Relationships of 2D Ruddlesden-Popper Tin- and Lead-based Iodide Perovskites. *ACS Appl. Mater. Interfaces* **2020**, *12*, 15328−15337.
(3) Ali, R.; Zhu, Z.-G.; Yan, Q.-B.; Zheng, Q.-R.; Su, G.; Laref, A.; Saraj, C. S.; Guo, C. Compositional Engineering Study of Lead-Free Hybrid Perovskites for Solar Cell Applications. *ACS Appl. Mater. Interfaces* **2020**, *12*, 49636−49647.
(4) Han, B.; Yuan, S.; Fang, T.; Zhang, F.; Shi, Z.; Song, J. Novel Lewis Base Cyclam Self-Passivation of Perovskites without An Anti-Solvent Process for Efficient Light-Emitting Diodes. *ACS Appl. Mater. Interfaces* **2020**, *12*, 14224−14232.
(5) Jena, A. K.; Kulkarni, A.; Miyasaka, T. Halide Perovskite Photovoltaics: Background, Status, and Future Prospects. *Chem. Rev.* **2019**, *119*, 3036−3103.
(6) Stranks, S. D.; Snaith, H. J. Metal-Halide Perovskites for Photovoltaic and Light-Emitting Devices. *Nat. Nanotechnol.* **2015**, *10*, 391−402.
(7) Quarti, C.; De Angelis, F.; Beljonne, D. Influence of Surface Termination on the Energy Level Alignment at the $CH_3NH_3PbI_3$ Perovskite/C_{60} Interface. *Chem. Mater.* **2017**, *29*, 958−968.
(8) Shi, R.; Vasenko, A. S.; Long, R.; Prezhdo, O. V. Edge Influence on Charge Carrier Localization and Lifetime in $CH_3NH_3PbBr_3$ Perovskite: Ab Initio Quantum Dynamics Simulation. *J. Phys. Chem. Lett.* **2020**, *11*, 9100−9109.
(9) Chu, W.; Saidi, W. A.; Zhao, J.; Prezhdo, O. V. Soft Lattice and Defect Covalency Rationalize Tolerance of β-$CsPbI_3$ Perovskite Solar Cells to Native Defects. *Angew. Chem., Int. Ed.* **2020**, *59*, 6435−6441.
(10) Chu, W.; Zheng, Q.; Prezhdo, O. V.; Zhao, J.; Saidi, W. A. Low-Frequency Lattice Phonons in Halide Perovskites Explain High Defect Tolerance Toward Electron-Hole Recombination. *Sci. Adv.* **2020**, *6*, No. eaaw7453.
(11) Kojima, A.; Teshima, K.; Shirai, Y.; Miyasaka, T. Organometal Halide Perovskites as Visible-Light Sensitizers for Photovoltaic Cells. *J. Am. Chem. Soc.* **2009**, *131*, 6050−6051.
(12) Quarti, C.; Marchal, N.; Beljonne, D. Tuning the Optoelectronic Properties of Two-Dimensional Hybrid Perovskite Semiconductors with Alkyl Chain Spacers. *J. Phys. Chem. Lett.* **2018**, *9*, 3416−3424.
(13) Noh, J. H.; Im, S. H.; Heo, J. H.; Mandal, T. N.; Seok, S. I. Chemical Management for Colorful, Efficient, and Stable Inorganic-Organic Hybrid Nanostructured Solar Cells. *Nano Lett.* **2013**, *13*, 1764−1769.
(14) Yu, W.; et al. Single Crystal Hybrid Perovskite Field-Effect Transistors. *Nat. Commun.* **2018**, *9*, No. 5354.
(15) Nan, G.; Beljonne, D.; Zhang, X.; Quarti, C. Organic Cations Protect Methylammonium Lead Iodide Perovskites against Small Exciton-Polaron Formation. *J. Phys. Chem. Lett.* **2020**, *11*, 2983−2991.
(16) Huang, J.; Yuan, Y.; Shao, Y.; Yan, Y. Understanding The Physical Properties of Hybrid Perovskites for Photovoltaic Applications. *Nat. Rev. Mater.* **2017**, *2*, No. 17042.
(17) Grätzel, M. The Light and Shade of Perovskite Solar Cells. *Nat. Mater.* **2014**, *13*, 838−842.
(18) Noel, N. K.; Stranks, S. D.; Abate, A.; Wehrenfennig, C.; Guarnera, S.; Haghighirad, A.-A.; Sadhanala, A.; Eperon, G. E.; Pathak, S. K.; Johnston, M. B.; Petrozza, A.; Herz, L. M.; Snaith, H. J. Lead-Free Organic-Inorganic Tin Halide Perovskites for Photovoltaic Applications. *Energy Environ. Sci.* **2014**, *7*, 3061−3068.
(19) Hao, F.; Stoumpos, C. C.; Chang, R. P.; Kanatzidis, M. G. Anomalous Band Gap Behavior in Mixed Sn and Pb Perovskites Enables Broadening of Absorption Spectrum in Solar Cells. *J. Am. Chem. Soc.* **2014**, *136*, 8094−8099.
(20) Yin, W. J.; Shi, T.; Yan, Y. Unique Properties of Halide Perovskites as Possible Origins of The Superior Solar Cell Performance. *Adv. Mater.* **2014**, *26*, 4653−4658.
(21) National Renewable Energy Laboratory. Best Research-Cell Efficiencies, 2020. https://www.nrel.gov/pv/cellefficiency.html.
(22) Lira-Cantú, M. Perovskite Solar Cells: Stability Lies at Interfaces. *Nat. Energy* **2017**, *2*, No. 17115.
(23) Battersby, S. News Feature: The Solar Cell of The Future. *Proc. Natl. Acad. Sci. U.S.A.* **2019**, *116*, 7−10.
(24) Chatterjee, S.; Pal, A. J. Influence of Metal Substitution on Hybrid Halide Perovskites: towards Lead-Free Perovskite Solar Cells. *J. Mater. Chem. A* **2018**, *6*, 3793−3823.
(25) Hao, F.; Stoumpos, C. C.; Liu, Z.; Chang, R. P.; Kanatzidis, M. G. Controllable Perovskite Crystallization at A Gas-Solid Interface for Hole Conductor-Free Solar Cells with Steady Power Conversion Efficiency over 10%. *J. Am. Chem. Soc.* **2014**, *136*, 16411−16419.
(26) Ju, M. G.; Sun, G.; Zhao, Y.; Liang, W. A Computational View of The Change in The Geometric and Electronic Properties of Perovskites Caused by The Partial Substitution of Pb by Sn. *Phys. Chem. Chem. Phys.* **2015**, *17*, 17679−17687.
(27) Song, T.-B.; Yokoyama, T.; Stoumpos, C. C.; Logsdon, J.; Cao, D. H.; Wasielewski, M. R.; Aramaki, S.; Kanatzidis, M. G. Importance of Reducing Vapor Atmosphere in The Fabrication of Tin-Based Perovskite Solar Cells. *J. Am. Chem. Soc.* **2017**, *139*, 836−842.
(28) Feng, J.; Xiao, B. Effective Masses and Electronic and Optical Properties of Nontoxic $MASnX_3$ (X = Cl, Br, and I) Perovskite Structures as Solar Cell Absorber: A Theoretical Study Using HSE06. *J. Phys. Chem. C* **2014**, *118*, 19655−19660.
(29) Stoumpos, C. C.; Frazer, L.; Clark, D. J.; Kim, Y. S.; Rhim, S. H.; Freeman, A. J.; Ketterson, J. B.; Jang, J. I.; Kanatzidis, M. G. Hybrid Germanium Iodide Perovskite Semiconductors: Active Lone Pairs, Structural Distortions, Direct and Indirect Energy Gaps, and Strong Nonlinear Optical Properties. *J. Am. Chem. Soc.* **2015**, *137*, 6804−6819.
(30) Kopacic, I.; Friesenbichler, B.; Hoefler, S. F.; Kunert, B.; Plank, H.; Rath, T.; Trimmel, G. Enhanced Performance of Germanium Halide Perovskite Solar Cells through Compositional Engineering. *ACS Appl. Energy Mater.* **2018**, *1*, 343−347.
(31) Umadevi, D.; Watson, G. W. Quasiparticle GW Calculations on Lead-Free Hybrid Germanium Iodide Perovskite $CH_3NH_3GeI_3$ for Photovoltaic Applications. *ACS Omega* **2019**, *4*, 5661−5669.
(32) Slavney, A. H.; Hu, T.; Lindenberg, A. M.; Karunadasa, H. I. A Bismuth-Halide Double Perovskite with Long Carrier Recombination Lifetime for Photovoltaic Applications. *J. Am. Chem. Soc.* **2016**, *138*, 2138−2141.
(33) McClure, E. T.; Ball, M. R.; Windl, W.; Woodward, P. M. Cs_2AgBiX_6 (X = Br, Cl): New Visible Light Absorbing, Lead-Free Halide Perovskite Semiconductors. *Chem. Mater.* **2016**, *28*, 1348−1354.
(34) Volonakis, G.; Filip, M. R.; Haghighirad, A. A.; Sakai, N.; Wenger, B.; Snaith, H. J.; Giustino, F. Lead-Free Halide Double Perovskites via Heterovalent Substitution of Noble Metals. *J. Phys. Chem. Lett.* **2016**, *7*, 1254−1259.
(35) Wei, F.; Deng, Z.; Sun, S.; Xie, F.; Kieslich, G.; Evans, D. M.; Carpenter, M. A.; Bristowe, P. D.; Cheetham, A. K. The Synthesis, Structure and Electronic Properties of A Lead-Free Hybrid Inorganic-Organic Double Perovskite $(MA)_2KBiCl_6$ (MA = methylammonium). *Mater. Horiz.* **2016**, *3*, 328−332.
(36) Filip, M. R.; Hillman, S.; Haghighirad, A. A.; Snaith, H. J.; Giustino, F. Band Gaps of The Lead-Free Halide Double Perovskites $Cs_2BiAgCl_6$ and $Cs_2BiAgBr_6$ from Theory and Experiment. *J. Phys. Chem. Lett.* **2016**, *7*, 2579−2585.

(37) Deng, Z.; Wei, F.; Sun, S.; Kieslich, G.; Cheetham, A. K.; Bristowe, P. D. Exploring The Properties of Lead-Free Hybrid Double Perovskites Using A Combined Computational-Experimental Approach. *J. Mater. Chem. A* **2016**, *4*, 12025−12029.
(38) Li, Y.-J.; Wu, T.; Sun, L.; Yang, R.-X.; Jiang, L.; Cheng, P.-F.; Hao, Q.-Q.; Wang, T.-J.; Lu, R.-F.; Deng, W.-Q. Lead-Free and Stable Antimony-Silver-Halide Double Perovskite $(CH_3NH_3)_2AgSbI_6$. *RSC Adv.* **2017**, *7*, 35175−35180.
(39) Pazoki, M.; Johansson, M. B.; Zhu, H.; Broqvist, P.; Edvinsson, T.; Boschloo, G.; Johansson, E. M. J. Bismuth Iodide Perovskite Materials for Solar Cell Applications: Electronic Structure, Optical Transitions, and Directional Charge Transport. *J. Phys. Chem. C* **2016**, *120*, 29039−29046.
(40) Volonakis, G.; Haghighirad, A. A.; Milot, R. L.; Sio, W. H.; Filip, M. R.; Wenger, B.; Johnston, M. B.; Herz, L. M.; Snaith, H. J.; Giustino, F. $Cs_2InAgCl_6$: A New Lead-Free Halide Double Perovskite with Direct Band Gap. *J. Phys. Chem. Lett.* **2017**, *8*, 772−778.
(41) Yang, B.; Chen, J.; Yang, S.; Hong, F.; Sun, L.; Han, P.; Pullerits, T.; Deng, W.; Han, K. Lead-Free Silver-Bismuth Halide Double Perovskite Nanocrystals. *Angew. Chem., Int. Ed.* **2018**, *57*, 5359−5363.
(42) Zhao, X. G.; Yang, J. H.; Fu, Y.; Yang, D.; Xu, Q.; Yu, L.; Wei, S. H.; Zhang, L. Design of Lead-Free Inorganic Halide Perovskites for Solar Cells via Cation-Transmutation. *J. Am. Chem. Soc.* **2017**, *139*, 2630−2638.
(43) Slavney, A. H.; Leppert, L.; Saldivar Valdes, A.; Bartesaghi, D.; Savenije, T. J.; Neaton, J. B.; Karunadasa, H. I. Small-Band-Gap Halide Double Perovskites. *Angew. Chem., Int. Ed.* **2018**, *57*, 12765−12770.
(44) Zhao, X. G.; Yang, D.; Sun, Y.; Li, T.; Zhang, L.; Yu, L.; Zunger, A. Cu-In Halide Perovskite Solar Absorbers. *J. Am. Chem. Soc.* **2017**, *139*, 6718−6725.
(45) Madan, J.; Shivani; Pandey, R.; Sharma, R. Device Simulation of 17.3% Efficient Lead-Free All-Perovskite Tandem Solar Cell. *Sol. Energy* **2020**, *197*, 212−221.
(46) Pantaler, M.; Cho, K. T.; Queloz, V. I. E.; García Benito, I.; Fettkenhauer, C.; Anusca, I.; Nazeeruddin, M. K.; Lupascu, D. C.; Grancini, G. Hysteresis-Free Lead-Free Double-Perovskite Solar Cells by Interface Engineering. *ACS Energy Lett.* **2018**, *3*, 1781−1786.
(47) Zhang, Y.; Yin, J.; Parida, M. R.; Ahmed, G. H.; Pan, J.; Bakr, O. M.; Bredas, J. L.; Mohammed, O. F. Direct-Indirect Nature of The Bandgap in Lead-Free Perovskite Nanocrystals. *J. Phys. Chem. Lett.* **2017**, *8*, 3173−3177.
(48) Liu, Q.; Liang, W. Structure and Property Tunability in Monolayer Halide Lead-Free Double Hybrid Perovskites: Effects of Rashba and Biaxial Strain. *J. Mater. Chem. A* **2019**, *7*, 11487−11496.
(49) Liu, Q.; Liang, W. How the Structures and Properties of Pristine and Anion Vacancy Defective Organic-Inorganic Hybrid Double Perovskites $MA_2AgIn(Br_xI_{1-x})_6$ Vary with Br Content x. *J. Phys. Chem. Lett.* **2020**, *11*, 10315−10322.
(50) Ali, R.; Hou, G.-J.; Zhu, Z.-G.; Yan, Q.-B.; Zheng, Q.-R.; Su, G. Stable Mixed Group II (Ca, Sr) and XIV (Ge, Sn) Lead-Free Perovskite Solar Cells. *J. Mater. Chem. A* **2018**, *6*, 9220−9227.
(51) Liu, M.; Pasanen, H.; Ali-Loytty, H.; Hiltunen, A.; Lahtonen, K.; Qudsia, S.; Smatt, J. H.; Valden, M.; Tkachenko, N. V.; Vivo, P. B-Site Co-Alloying with Germanium Improves The Efficiency and Stability of All-Inorganic Tin-Based Perovskite Nanocrystal Solar Cells. *Angew. Chem., Int. Ed.* **2020**, *59*, 22117−22125.
(52) Ma, X.-X.; Li, Z.-S. Influence of Sn/Ge Cation Exchange on Vacancy-Ordered Double Perovskite $Cs_2Sn_{(1-x)}Ge_xI_6$: A First-Principles Theoretical Study. *Phys. Status Solidi B* **2019**, *256*, No. 1800427.
(53) Minemoto, T.; Kawano, Y.; Nishimura, T.; Shen, Q.; Yoshino, K.; Iikubo, S.; Hayase, S.; Chantana, J. Theoretical Analysis of Band Alignment at Back Junction in Sn−Ge Perovskite Solar Cells with Inverted p-i-n Structure. *Sol. Energy Mater. Sol. Cells* **2020**, *206*, No. 110268.
(54) Ng, C. H.; Nishimura, K.; Ito, N.; Hamada, K.; Hirotani, D.; Wang, Z.; Yang, F.; likubo, S.; Shen, Q.; Yoshino, K.; Minemoto, T.; Hayase, S. Role of GeI_2 and SnF_2 Additives for SnGe Perovskite Solar Cells. *Nano Energy* **2019**, *58*, 130−137.
(55) Qian, F.; Hu, M.; Gong, J.; Ge, C.; Zhou, Y.; Guo, J.; Chen, M.; Ge, Z.; Padture, N. P.; Zhou, Y.; Feng, J. Enhanced Thermoelectric Performance in Lead-Free Inorganic $CsSn_{(1-x)}Ge_xI_3$ Perovskite Semiconductors. *J. Phys. Chem. C* **2020**, *124*, 11749−11753.
(56) Zou, S.; Liu, Y.; Li, J.; Liu, C.; Feng, R.; Jiang, F.; Li, Y.; Song, J.; Zeng, H.; Hong, M.; Chen, X. Stabilizing Cesium Lead Halide Perovskite Lattice through Mn(II) Substitution for Air-Stable Light-Emitting Diodes. *J. Am. Chem. Soc.* **2017**, *139*, 11443−11450.
(57) Tavakoli, M. M.; Zakeeruddin, S. M.; Grätzel, M.; Fan, Z. Large-Grain Tin-Rich Perovskite Films for Efficient Solar Cells via Metal Alloying Technique. *Adv. Mater.* **2018**, *30*, No. 1705998.
(58) Zuo, F.; Williams, S. T.; Liang, P.-W.; Chueh, C.-C.; Liao, C.-Y.; Jen, A. K.-Y. Binary-Metal Perovskites Toward High-Performance Planar-Heterojunction Hybrid Solar Cells. *Adv. Mater.* **2014**, *26*, 6454−6460.
(59) Tsai, C.-M.; Wu, H.-P.; Chang, S.-T.; Huang, C.-F.; Wang, C.-H.; Narra, S.; Yang, Y.-W.; Wang, C.-L.; Hung, C.-H.; Diau, E. W.-G. Role of Tin Chloride in Tin-Rich Mixed-Halide Perovskites Applied as Mesoscopic Solar Cells with a Carbon Counter Electrode. *ACS Energy Lett.* **2016**, *1*, 1086−1093.
(60) Ogomi, Y.; Morita, A.; Tsukamoto, S.; Saitho, T.; Fujikawa, N.; Shen, Q.; Toyoda, T.; Yoshino, K.; Pandey, S. S.; Ma, T.; Hayase, S. $CH_3NH_3Sn_xPb_{(1-x)}I_3$ Perovskite Solar Cells Covering up to 1060 nm. *J. Phys. Chem. Lett.* **2014**, *5*, 1004−1011.
(61) Ju, M. G.; Dai, J.; Ma, L.; Zeng, X. C. Lead-Free Mixed Tin and Germanium Perovskites for Photovoltaic Application. *J. Am. Chem. Soc.* **2017**, *139*, 8038−8043.
(62) Ito, N.; Kamarudin, M. A.; Hirotani, D.; Zhang, Y.; Shen, Q.; Ogomi, Y.; Iikubo, S.; Minemoto, T.; Yoshino, K.; Hayase, S. Mixed Sn−Ge Perovskite for Enhanced Perovskite Solar Cell Performance in Air. *J. Phys. Chem. Lett.* **2018**, *9*, 1682−1688.
(63) Blöchl, P. E. Projector Augmented-Wave Method. *Phys. Rev. B* **1994**, *50*, 17953−17979.
(64) Kresse, G. Ab-Initio Molecular-Dynamics for Liquid-Metals. *J. Non-Cryst. Solids* **1995**, *192*−*193*, 222−229.
(65) Perdew, J. P.; Burke, K.; Ernzerhof, M. Generalized Gradient Approximation Made Simple. *Phys. Rev. Lett.* **1996**, *77*, 3865−3868.
(66) Heyd, J.; Scuseria, G. E.; Ernzerhof, M. Hybrid Functionals Based on A Screened Coulomb Potential. *J. Chem. Phys.* **2003**, *118*, 8207.
(67) Chu, W.; Zheng, Q.; Akimov, A. V.; Zhao, J.; Saidi, W. A.; Prezhdo, O. V. Accurate Computation of Nonadiabatic Coupling with Projector Augmented-Wave Pseudopotentials. *J. Phys. Chem. Lett.* **2020**, *11*, 10073−10080.
(68) Akimov, A. V.; Prezhdo, O. V. The PYXAID Program for Non-Adiabatic Molecular Dynamics in Condensed Matter Systems. *J. Chem. Theory Comput.* **2013**, *9*, 4959−4972.
(69) Akimov, A. V.; Prezhdo, O. V. Advanced Capabilities of The PYXAID Program: Integration Schemes, Decoherence Effects, Multiexcitonic States, and Field-Matter Interaction. *J. Chem. Theory Comput.* **2014**, *10*, 789−804.
(70) Shi, C.; Yu, C. H.; Zhang, W. Predicting and Screening Dielectric Transitions in a Series of Hybrid Organic-Inorganic Double Perovskites via an Extended Tolerance Factor Approach. *Angew. Chem., Int. Ed.* **2016**, *55*, 5798−5802.
(71) Kieslich, G.; Sun, S.; Cheetham, A. K. An Extended Tolerance Factor Approach for Organic-Inorganic Perovskites. *Chem. Sci.* **2015**, *6*, 3430−3433.
(72) Travis, W.; Glover, E. N. K.; Bronstein, H.; Scanlon, D. O.; Palgrave, R. G. On The Application of The Tolerance Factor to Inorganic and Hybrid Halide Perovskites: A Revised System. *Chem. Sci.* **2016**, *7*, 4548−4556.
(73) Wang, K.; Liang, Z.; Wang, X.; Cui, X. Lead Replacement in $CH_3NH_3PbI_3$ Perovskites. *Adv. Electron. Mater.* **2015**, *1*, No. 150089.
(74) Hao, F.; Stoumpos, C. C.; Cao, D. H.; Chang, R. P. H.; Kanatzidis, M. G. Lead-Free Solid-State Organic-Inorganic Halide Perovskite Solar Cells. *Nat. Photonics* **2014**, *8*, 489−494.

https://doi.org/10.1021/acsami.1c03145
ACS Appl. Mater. Interfaces 2021, 13, 16567−16575

(75) Quarti, C.; Grancini, G.; Mosconi, E.; Bruno, P.; Ball, J. M.; Lee, M. M.; Snaith, H. J.; Petrozza, A.; Angelis, F. D. The Raman Spectrum of The $CH_3NH_3PbI_3$ Hybrid Perovskite: Interplay of Theory and Experiment. *J. Phys. Chem. Lett.* **2014**, *5*, 279−284.
(76) Leguy, A. M.; Goni, A. R.; Frost, J. M.; Skelton, J.; Brivio, F.; Rodriguez-Martinez, X.; Weber, O. J.; Pallipurath, A.; Alonso, M. I.; Campoy-Quiles, M.; Weller, M. T.; Nelson, J.; Walsh, A.; Barnes, P. R. Dynamic Disorder, Phonon Lifetimes, and The Assignment of Modes to The Vibrational Spectra of Methylammonium Lead Halide Perovskites. *Phys. Chem. Chem. Phys.* **2016**, *18*, 27051−27066.
(77) Justo, J. F.; de Brito Mota, F.; Fazzio, A. First-Principles Investigation of a-SiN_x:H. *Phys. Rev. B* **2002**, *65*, No. 073202.
(78) Ashhab, S.; Voznyy, O.; Hoogland, S.; Sargent, E. H.; Madjet, M. E. Effect of Disorder on Transport Properties in A Tight-Binding Model for Lead Halide Perovskites. *Sci. Rep.* **2017**, *7*, No. 8902.
(79) Mukamel, S. *Principles of Nonlinear Optical Spectroscopy*; Oxford University Press: New York, 1995; Vol. *29*.
(80) Kilina, S. V.; Neukirch, A. J.; Habenicht, B. F.; Kilin, D. S.; Prezhdo, O. V. Quantum Zeno Effect Rationalizes The Phonon Bottleneck in Semiconductor Quantum Dots. *Phys. Rev. Lett.* **2013**, *110*, No. 180404.

https://doi.org/10.1021/acsami.1c03145
ACS Appl. Mater. Interfaces 2021, 13, 16567−16575